Research Square

Preprints are preliminary reports that have not undergone peer review.
They should not be considered conclusive, used to inform clinical practice,
or referenced by the media as validated information.

Eliminating catalyst-membrane interfacial discontinuity for alkaline water electrolysis

Jianguo Liu

jianguoliu@ncepu.edu.cn

North China Electric Power University https://orcid.org/0000-0002-9229-4936

Shukai Diao

North China Electric Power University

Senlin Li

North China Electric Power University

Zhonghao Li

North China Electric Power University

Ying Liu

North China Electric Power University

Tianrang Yang

North China Electric Power University https://orcid.org/0000-0003-0843-4236

Article

Keywords:

Posted Date: August 24th, 2026

DOI: https://doi.org/10.21203/rs.3.rs-10467834/v1

License: This work is licensed under a Creative Commons Attribution 4.0 International License.
Read Full License

Additional Declarations: There is **NO** Competing Interest.

Eliminating catalyst-membrane interfacial discontinuity for alkaline water electrolysis

Shukai Diao[1,2,3], Senlin Li[1,2,3], Zhonghao Li[1,2,3], Ying Liu[1,2,3], Tianrang Yang[1,2*], Jianguo Liu[1,2*]

[1]*Beijing Laboratory of New Energy Storage Technology, Institute of Energy Power Innovation, North China Electric Power University, Beijing 102206, P.R. China*

[2]*Beijing Key Laboratory of Electrochemical Hydrogen Production and Fuel Cells, North China Electric Power University, Beijing 102206, China*

[3]*School of Energy Power and Mechanical Engineering, North China Electric Power University, Beijing 102206, PR China*

**Corresponding author: tianrangyang@ncepu.edu.cn; jianguoliu@ncepu.edu.cn*

Abstract

Thick porous membranes limit gas crossover in alkaline water electrolysis but introduce substantial ohmic losses at industrial current densities, whereas thinning them increases hydrogen-to-oxygen (HTO) crossover. Here we show that this coupled limitation is not dictated solely by membrane thickness, but is strongly influenced by gas accumulation at the discontinuous catalyst-membrane interface. This interfacial gas retention increases local ionic resistance and facilitates hydrogen transport across the membrane. We remove this interfacial discontinuity by co-forming the catalyst layer and membrane through a synchronized phase-inversion process, embedding NiAl catalysts and ZrO_2 fillers within a shared three-dimensional polysulfone scaffold. The resulting integrated catalyst-membrane (ICM) electrolyzer reaches 2.05 A cm^{-2} at 1.8 V using a 480-μm membrane, while suppressing HTO crossover and operating stably for 8000 h with a decay rate of 1.9 μV h^{-1}. Our results establish interfacial continuity as a design parameter for managing resistance and crossover in alkaline water electrolysis.

Introduction

Progress in alkaline water electrolysis has established it a promising route for large-scale green hydrogen production[1-3]. Its performance depends on two coupled but often separately optimized functions, namely efficient electrochemical conversion at the electrodes and reliable gas blocking by the membrane[4,5]. Advances in nickel-based catalysts have reduced reaction overpotentials, while asbestos-free porous composite membranes, represented by ZrO_2-filled polysulfone membranes, have improved ionic conduction and gas blocking[6-8]. To further reduce ohmic loss, decreasing membrane thickness has become a prevalent strategy because it shortens the ion-transport pathway and lowers area resistance[9-11]. However, thinner membranes are more susceptible to mechanical deformation, hydrogen-to-oxygen (HTO) crossover and durability loss under industrially relevant current densities and pressure gradients[12-14]. Practical alkaline electrolyzers therefore remain constrained by the competing requirements of low ionic resistance and safe gas separation[15-17].

This trade-off is usually attributed to the bulk membrane, yet modern zero-gap alkaline electrolyzers introduce an additional source of loss at the buried catalyst-membrane interface[18-20]. Although close electrode-membrane contact shortens the ionic transport pathway, mechanically assembling independently fabricated components creates a intrinsically discontinuous boundary[21,22]. Electrode roughness, membrane

deformation and nonuniform compression generate microscopic voids and poorly wetted regions at the interface[23,24]. At high current density, rapidly evolved gas bubbles can enter or remain trapped in these interfacial defects, forming gas-filled pockets that block electrolyte access and interrupt ion transport[25,26]. These gas-retention zones behave as local insulating regions, contributing to current-dependent interfacial resistance while also promoting hydrogen transport across the membrane[27,28]. Thus, the apparent resistance-crossover trade-off is not governed solely by membrane thickness but also by the structural continuity of the catalyst-membrane interface.

Several approaches have attempted to reduce this interfacial penalty by bringing catalytic and membrane functions closer together[29]. Catalyst-coated membranes reduce the apparent electrode-membrane distance by placing a catalytic layer directly on a preformed membrane surface[30]. However, these structures are typically prepared through sequential coating, spraying or electrodeposition onto an existing membrane[19]. Differences in binder chemistry, porosity and mechanical response between the catalytic layer and the membrane limit interpenetration across the boundary, leaving the interface dominated by physical adhesion rather than a continuous structural integration. This residual boundary remains vulnerable to gas accumulation, delamination and structural degradation during prolonged gas evolution.

Here, we report an integrated catalyst-membrane architecture formed through a synchronized phase-inversion process. NiAl catalyst layer and ZrO_2-containing membrane precursors are co-cast from a shared solvent system and undergo simultaneous demixing, generating a continuous three-dimensional polysulfone scaffold across the catalytic and membrane domains. This monolithic architecture removes the discrete physical boundary between the catalyst layer and membrane, suppresses interfacial gas retention, and reduces current-dependent ionic resistance without relying on membrane thinning. As a result, the integrated electrolyzer achieves 2.05 A cm^{-2} at 1.80 V using a robust 480-μm membrane while maintaining suppressed HTO crossover. It operates for more than 8000 h with a decay rate of 1.9 μV h^{-1}. The techno-economic analysis indicates a levelized cost of US$0.915 kg^{-1} H_2, highlighting interfacial-continuity engineering as a scalable design principle for the next-generation alkaline water electrolysis.

Results

Interfacial losses in conventional zero-gap alkaline electrolyzers

In conventional zero-gap alkaline electrolyzers, porous membranes and electrodes are fabricated separately and brought into contact by mechanical compression. This nominally zero-gap configuration therefore still contains a discrete electrode-membrane interface, where local voids and contact resistance can introduce additional ohmic losses, particularly during high-current gas evolution. Such interfacial losses can restrict attainable current density, increase energy consumption and compromise gas purity. To examine these limitations, alkaline water electrolyzers were assembled using commercial polyphenylene sulfide (PPS) and Zirfon 500 membranes. Electrochemical impedance spectroscopy (EIS) was performed at open-circuit voltage, 1.8 V and 2.0 V, and the resulting Nyquist plots were used to determine the cell ohmic resistance (Supplementary Fig. S1a,b). The polarization curves were further deconvoluted into kinetic, ohmic and mass-transport overpotentials (Supplementary Fig. S1c,d).

For both membranes, the ohmic resistance increased with cell voltage, leading to a larger ohmic contribution at higher current densities. For PPS, the ohmic overpotential increased from 11.0% of the total overpotential at 1.8 V to 28.7% at 2.0 V. Although Zirfon 500 showed a lower overall resistance owing to its smaller thickness and greater wettability, its ohmic contribution still increased from 10.3% to 25.3% over the same voltage range. This current-dependent rise in resistance indicates that lowering the bulk membrane resistance alone is insufficient to eliminate the ohmic penalty under intensified gas evolution, underscoring the need to engineer the electrode-membrane interface.

Fabrication and interfacial architecture of the ICM

To overcome the interfacial limitations of mechanically assembled electrode-membrane configurations, we developed an integrated catalyst-membrane, denoted as ICM, in which the catalyst layer and membrane are formed as a continuous monolithic structure. As illustrated in Fig. 1a, a catalyst slurry containing NiAl particles, polysulfone (PSU) and polyvinylpyrrolidone (PVP) in N-methyl-2-pyrrolidone (NMP) was first cast onto a glass substrate. After controlled solvent evaporation, a membrane-forming slurry composed of ZrO_2, PSU and PVP in NMP was directly cast onto the catalyst layer. The bilayer precursor then underwent pre-evaporation and phase inversion in water to yield the ICM.

Because the catalyst and membrane precursors shared the same solvent system and underwent coupled phase inversion before complete solidification, the two layers were integrated through a continuous PSU framework rather than being joined by post-fabrication mechanical contact. The resulting ICM exhibited distinct membrane-side and catalyst-side surfaces and could be fabricated over a large area of 8 cm × 26 cm (Fig. 1b). It could also be folded without visible cracking or delamination, indicating mechanical flexibility and structural integrity (Fig. 1c). Top-view SEM images showed a relatively dense membrane-side surface and a porous catalyst-layer side with exposed NiAl particles embedded within the polymer framework (Fig. 1d).

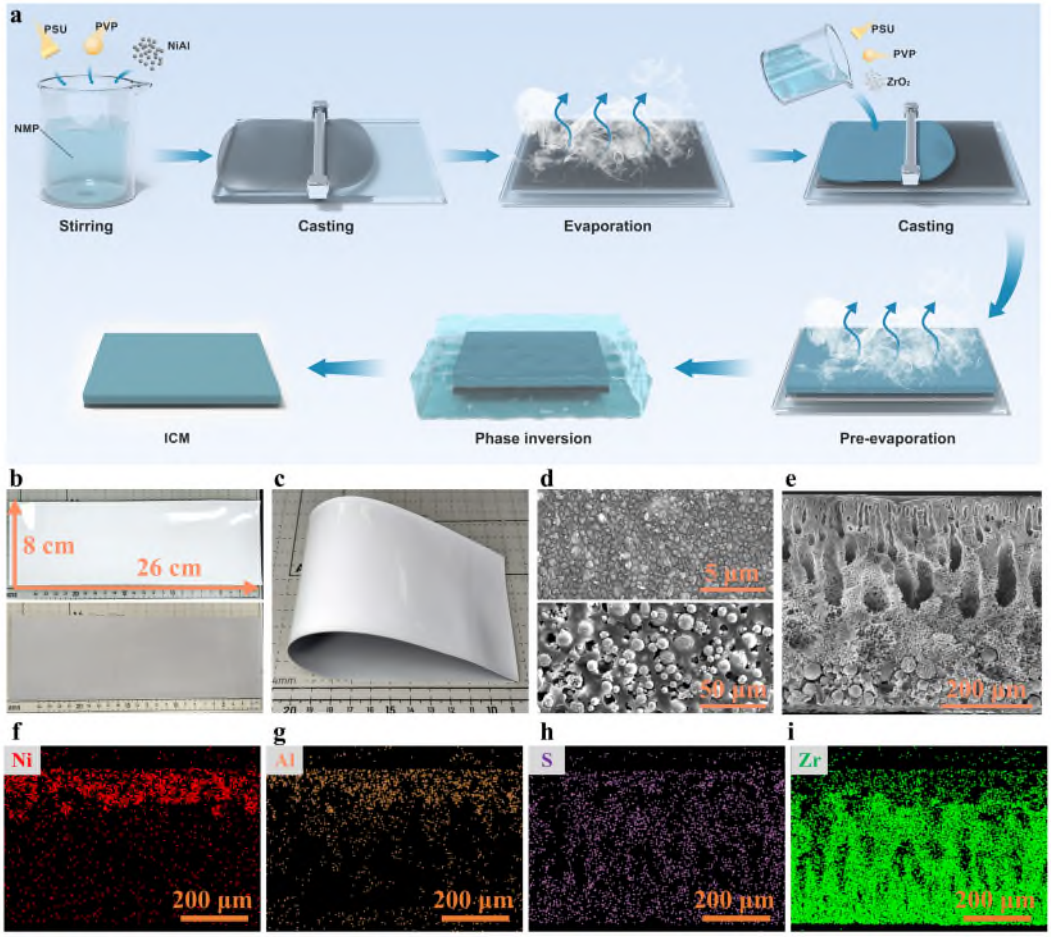


Fig. 1 Fabrication and structural characterization of the ICM. a, Schematic illustration of the ICM fabrication process. **b,** Digital photographs of the membrane side and catalyst-layer side of the ICM. **c,** Digital photograph of the folded ICM, demonstrating its mechanical flexibility. **d,** Top-view SEM images of the membrane side and catalyst side of the ICM. **e,** Cross-sectional SEM image of the ICM. **f-i,** Corresponding EDS elemental maps of Ni (**f**), Al (**g**), S (**h**) and Zr (**i**) acquired from the region in **e**.

Cross-sectional SEM revealed an asymmetric architecture comprising a dense membrane surface, a finger-like porous membrane region and a catalyst layer, with no discernible gap or delamination at the catalyst-membrane interface (Fig. 1e and Supplementary Fig. S2). EDS mapping showed that Ni and Al were concentrated in the catalyst layer, whereas Zr was mainly distributed throughout the membrane region (Fig. 1f,g,i). Notably, the S signal from the PSU matrix extended continuously across both regions, supporting the formation of an interconnected polymer framework across the catalyst-membrane interface (Fig. 1h).

The origin of this asymmetric membrane structure was clarified using a catalyst-free ZrO_2-PSU membrane, denoted as ZP, prepared by the same phase-inversion process. ZP exhibited a dense skin layer on the upper surface and an open porous structure on the glass-contacting side (Supplementary Fig. S3a-c), a morphology favorable for ICM construction because the dense upper layer preserves gas separation while the porous underside promotes interconnection with the catalyst layer. To verify that the continuous catalyst-membrane interface originated from coupled phase inversion rather than simple physical contact between two porous layers, we prepared a control catalyst-laminated membrane, denoted as CLM. In this control, the membrane and catalyst layers were first fabricated separately and then joined by hot pressing. Although the CLM exhibited surface morphologies similar to the ICM, its cross-section showed a distinct interfacial boundary with local voids (Supplementary Fig. S3d-f), demonstrating that post-fabrication lamination cannot reproduce the continuous interface formed by coupled phase inversion.

Catalyst evolution and membrane properties of the ICM

The ICM must combine catalytic functionality with the ion-transport and gas-separation properties required for alkaline water electrolysis. Because the NiAl catalyst layer undergoes alkaline activation before operation, its structural evolution was examined in the fresh state, after KOH activation and after 10 days of electrolysis. The fresh catalyst layer mainly contained Ni_2Al_3 and metallic Al (Supplementary Fig. S4). KOH activation removed the Al-rich phases and generated a reconstructed Ni/NiAl-containing structure (Fig. 2a and Supplementary Fig. S5), whereas subsequent electrolysis produced α- and β-$Ni(OH)_2$ features and dominant Ni^{2+} surface species while retaining residual NiAl regions (Fig. 2b,c). TEM analysis further showed that operation transformed the initially particulate catalyst into a nanosheet-covered architecture, with lattice spacings assigned to β-$Ni(OH)_2$ and NiAl (Fig. 2d-f). These

results indicate that the integrated NiAl layer evolves into a Ni/Ni(OH)$_2$-rich active structure during alkaline operation while maintaining residual NiAl regions within the monolithic framework.

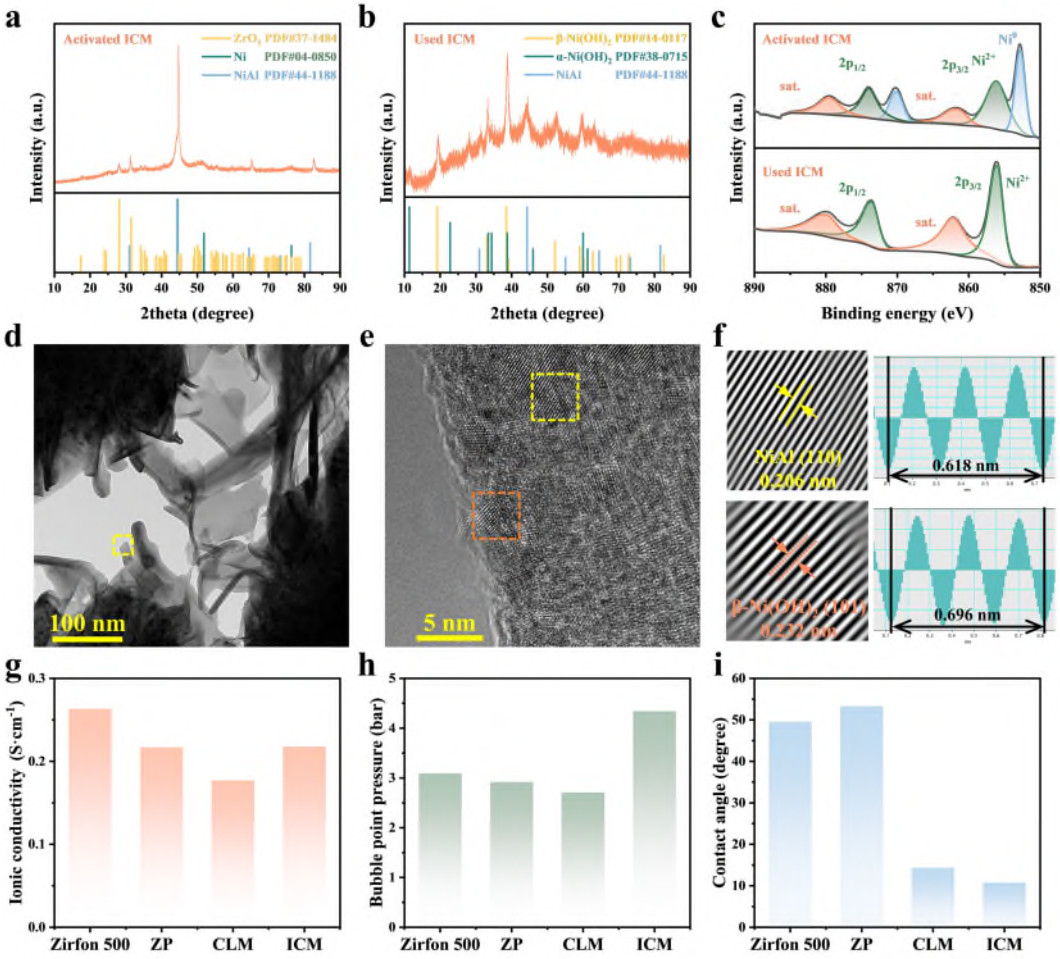


Fig. 2 Structural evolution of the catalyst layer and membrane-related properties of the ICM. a, b, X-ray diffraction patterns collected from the catalyst-layer side of the ICM after KOH activation (**a**) and after 10 days of electrolyzer operation (**b**), together with the corresponding reference patterns. **c,** High-resolution Ni 2p XPS spectra collected from the catalyst-layer side of the activated ICM and the ICM after 10 days of operation. **d-f,** TEM image (**d**), HRTEM image (**e**) and filtered lattice-fringe images with the corresponding line-intensity profiles (**f**) of the catalyst layer after 10 days of operation. **g-i,** Ionic conductivity (**g**), bubble point pressure (**h**) and water contact angle (**i**) of Zirfon 500, ZP, CLM and ICM.

The membrane-related properties of the ICM were then evaluated against Zirfon 500, ZP and CLM. Through-plane ionic conductivity was obtained from area-specific resistance measurements in an H-type cell (Supplementary Fig. S6). The CLM showed reduced ionic conductivity because the laminated catalyst layer introduced additional

ion-transport resistance, whereas the ICM maintained a conductivity close to that of catalyst-free ZP despite its integrated catalyst layer and comparable overall thickness (Fig. 2g). The ICM also exhibited the highest bubble-point pressure, indicating improved resistance to gas penetration (Fig. 2h). Contact-angle measurements performed on the catalyst-facing side showed that the ICM had the greatest wettability, favoring electrolyte infiltration and continuous ionic contact (Fig. 2i). FTIR spectra confirmed that catalyst integration did not alter the chemical functional groups of the PSU-based membrane matrix, while pore-size and water-uptake measurements showed that the ICM combined smaller pores with higher water uptake than the CLM (Supplementary Fig. S7). Collectively, these results demonstrate that the ICM preserves membrane functions of ionic conduction and gas blocking while enabling the NiAl catalyst layer to reconstruct into an active Ni/$Ni(OH)_2$-rich structure.

Electrochemical performance of the ICM electrolyzers

The electrochemical role of the integrated NiAl catalyst layer was first evaluated to determine the optimal ICM orientation. Because the membrane component is electronically insulating, an independently cast catalyst layer was hot-pressed onto Ni felt to form a catalyst-coated substrate, denoted as CCS-Ni felt. Compared with bare Ni felt, CCS-Ni felt showed enhanced HER activity but lower OER activity (Supplementary Fig. S8a,b), indicating that the NiAl layer is better suited for hydrogen evolution reaction. Consistently, electrolyzers assembled with the ICM catalyst layer facing the cathode exhibited better polarization performance and lower impedance than those with the catalyst layer facing the anode (Supplementary Fig. S8c,d). Therefore, the ICM was installed with its catalyst layer facing the cathode in all subsequent tests.

As illustrated in Fig. 3a, the integrated catalyst layer served as the HER-active cathode, while the adjacent Ni foam functioned mainly as the porous transport layer (PTL) and current collector. Bare Ni foam was used as the oxygen-evolution electrode on the anode side. The continuous catalyst-membrane interface in the ICM promotes electrolyte access, provides connected pathways for H_2 removal and eliminates the mechanically contacted boundary, while the finger-like membrane pores facilitate OH^- transport and the dense skin layer suppresses gas crossover (Fig. 3b).

The electrochemical contribution of each cell component was then evaluated using a series of progressively optimized configurations (Fig.3c,d). For clarity, the conventional mechanically assembled cells are abbreviated as NF/PPS/NF, NF/ZF/NF and NF/ZF/RN, where NF, ZF and RN denote Ni foam, Zirfon 500 and Raney Ni,

respectively. The baseline NF/PPS/NF cell required 2.24 V to reach 1.0 A cm^{-2}. Replacing PPS with ZF reduced the voltage to 2.12 V, mainly due to the lower area resistance of ZF. Further introducing RN as the cathodic catalyst decreased the voltage to 1.97 V by increasing the HER-active surface area.

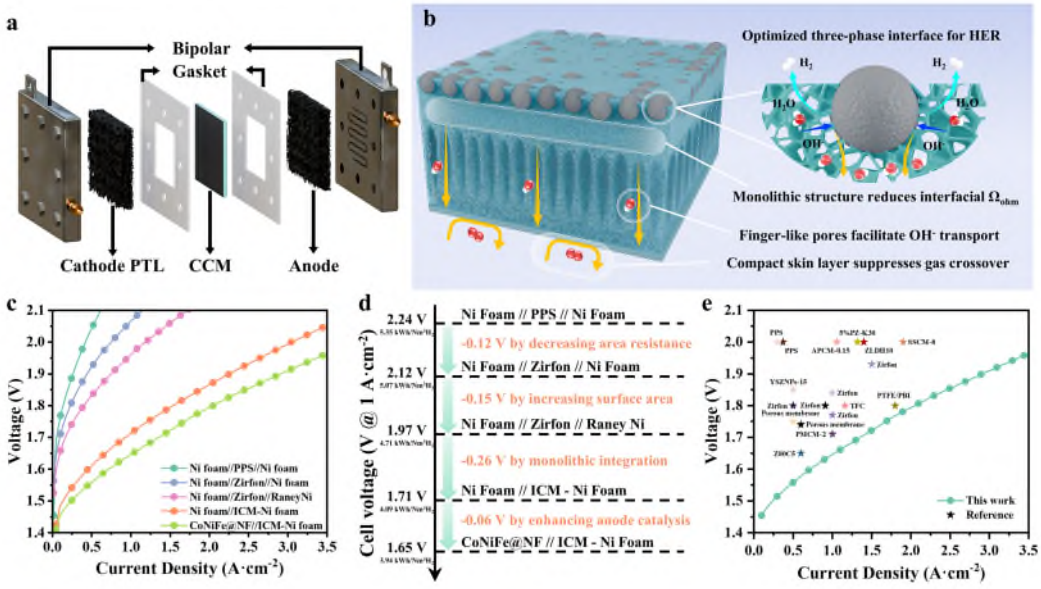


Fig. 3 Configuration and electrochemical performance of the ICM-based alkaline water electrolyzer. a, Exploded schematic of the alkaline electrolyzer assembled with the ICM. **b,** Schematic illustration of the ICM structure and its functional features during electrolysis. **c,** Polarization curves of alkaline electrolyzers with different anode/membrane/cathode configurations. **d,** Cell voltage and corresponding energy consumption for hydrogen production at 1.0 A cm^{-2} for the different cell configurations. **e,** Comparison of the polarization performance of the ICM-based electrolyzer with previously reported alkaline water electrolyzers.

In comparison, the ICM cell with bare NF anode, abbreviated as NF/ICM/NF, required only 1.71 V at 1.0 A cm^{-2}. This pronounced decrease highlights the key role of monolithic catalyst-membrane integration in reducing interfacial losses beyond what can be achieved by simply lowering membrane resistance or increasing catalyst surface area. To further assess scalability, the active area of the NF/ICM/NF cell was enlarged to 10 cm × 10 cm. The enlarged electrolyzer reached 1.0 A cm^{-2} at 1.74 V, showing only a modest performance loss relative to the small-area cell (Supplementary Fig. S10).

Replacing the anode with CoNiFe@NF further reduced the voltage to 1.65 V at 1.0 A cm^{-2} and delivered 2.05 A cm^{-2} at 1.80 V, exceeding the DOE 2026 performance target of 1.0 A cm^{-2} at 1.80 V. The hydrogen-production energy consumption was

accordingly decreased from 4.71 kWh Nm^{-3} H_2 for NF/ZF/RN to 4.08 and 3.94 kWh Nm^{-3} H_2 for NF/ICM/NF and CoNiFe@NF/ICM/NF, respectively. Compared with recently reported alkaline water electrolyzers, the ICM electrolyzer delivered favorable high-current performance over the examined voltage range (Fig. 3e and Supplementary Table 1).

Interfacial continuity reduces ohmic loss and H_2 crossover

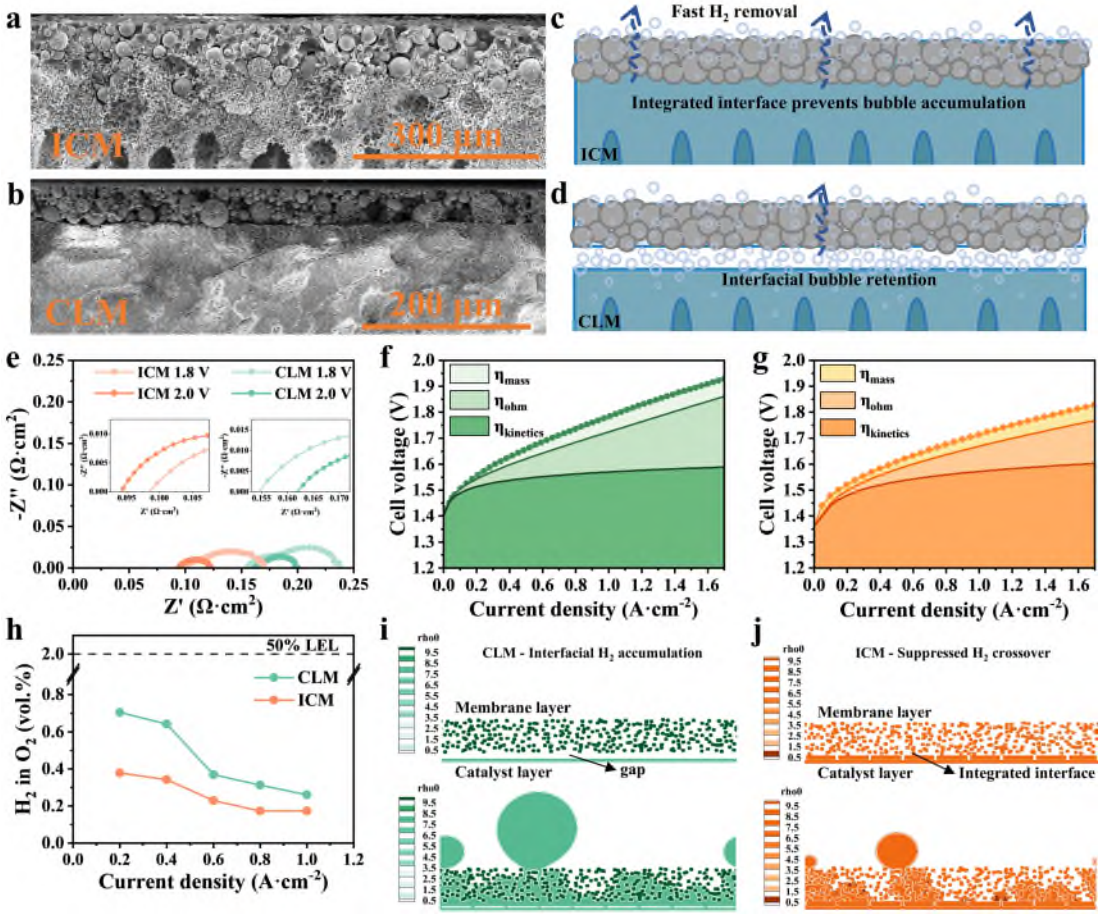


Fig. 4 Comparison of interfacial transport and gas crossover in ICM and CLM. a, b, Cross-sectional SEM images of the catalyst-membrane interfaces in ICM (**a**) and CLM (**b**). **c, d,** Schematic illustrations of hydrogen removal at the integrated ICM interface (**c**) and hydrogen retention at the laminated CLM interface (**d**). **e,** Nyquist plots of ICM- and CLM-based electrolyzers measured at 1.8 and 2.0 V. **f, g,** Deconvolution of the polarization curves into kinetic, ohmic and mass transport overpotentials for the CLM- (**f**) and ICM-based (**g**) electrolyzers. **h,** Hydrogen concentration in the oxygen product gas at different current densities. **i, j,** Simulated hydrogen concentration distributions during crossover through CLM (**i**) and ICM (**j**).

To directly evaluate the benefit of catalyst-membrane interfacial continuity, the ICM and CLM were compared, revealing markedly different cross-sectional structures.

The ICM showed a continuous transition between the catalyst and membrane regions without an evident interfacial gap (Fig. 4a), whereas the CLM retained a distinct boundary with local voids between the separately formed layers (Fig. 4b). This comparison therefore isolates the role of interfacial continuity.

As illustrated in Fig. 4c, d, the continuous ICM interface provides direct pathways for electrolyte supply and H_2 removal, reducing the tendency for bubbles to accumulate between the catalyst layer and membrane (Fig. 4c). In contrast, the discontinuous CLM interface creates confined interfacial spaces that can retain evolved H_2, locally displace electrolyte and interrupt ionic contact (Fig. 4d). Such gas-filled interfacial voids are expected to increase interfacial ohmic loss, particularly at high current densities. At both 1.8 and 2.0 V, the ICM electrolyzer exhibited smaller high-frequency intercepts and polarization arcs than the CLM, corresponding to lower ohmic and polarization resistances despite operating at higher current densities (Fig. 4e). Moreover, the ohmic resistance of the ICM electrolyzer remained nearly unchanged as the voltage increased from 1.8 to 2.0 V, whereas that of the CLM increased noticeably. This contrast indicates that the integrated interface suppresses the current-dependent increase in ohmic resistance associated with intensified gas evolution and interfacial bubble retention.

Overpotential deconvolution further confirmed that the improvement arose mainly from reduced ohmic loss (Fig. 4f,g). For the CLM electrolyzer, the ohmic contribution increased from 17.6% of the total overpotential at 0.5 A cm^{-2} to 28.0% at 1.0 A cm^{-2}, compared with 12.4% and 19.9% for the ICM. The kinetic overpotentials remained comparable, indicating similar intrinsic catalytic activity. The superior ICM performance therefore originates primarily from lower ohmic loss, together with reduced mass-transport loss, rather than altered catalyst activity.

Gas crossover was then evaluated by monitoring the H_2 concentration in the oxygen product gas. Across the investigated current-density range, the ICM consistently exhibited lower H_2-in-O_2 concentration than the CLM (Fig. 4h). For both configurations, the measured H_2-in-O_2 concentration decreased with increasing current density, largely because increased oxygen production diluted the crossed-over hydrogen. Nevertheless, the consistently lower values obtained with the ICM show that the integrated architecture more effectively suppresses hydrogen crossover.

To clarify the structural origin of this difference, physical models of the CLM and ICM were constructed from their cross-sectional morphologies, and transient two-phase H_2 transport in 30 wt% KOH was simulated using the lattice Boltzmann method. A 10

μm interfacial gap was introduced in the CLM model to represent the mechanically laminated boundary, whereas the ICM model contained a continuous catalyst-membrane interface (Fig. 4i,j). In the CLM, the interfacial gap provided a confined region for bubble retention and local H_2 enrichment, increasing gas accumulation adjacent to the membrane and strengthening the driving force for crossover. By contrast, the continuous porous framework of the ICM facilitated H_2 removal from the interface and reduced local gas accumulation. The simulated through-plane gas-saturation profiles further showed lower gas saturation near the membrane in the ICM than in the CLM, consistent with the H_2-in-O_2 measurements (Supplementary Fig. S11).

Durability and economic assessment of the ICM electrolyzers

The NF/ICM/NF electrolyzer operated continuously for over 8,000 h at 1.08 A cm^{-2}, exhibiting an average voltage degradation rate of only 1.9 μV h^{-1} (Fig. 5a). This value is lower than both the DOE 2026 and ultimate average degradation-rate benchmarks of 2.3 and 2.1 μV h^{-1}, respectively. Using the DOE end-of-life criterion, defined as a 10% increase relative to the beginning-of-life voltage after conditioning, the measured degradation rate and a beginning-of-life voltage of approximately 1.75 V correspond to a projected lifetime of about 92,000 h under this degradation-rate assumption, exceeding the DOE lifetime target of 80,000 h. Periodic impedance measurements showed no appreciable increase in ohmic resistance, indicating retention of interfacial contact and electrolyte-filled ion-transport pathways during prolonged gas-evolving operation. Compared with recently reported alkaline water electrolysis systems, the ICM combines a relatively large membrane thickness with an extended high-current stability (Fig. 5b).

The ICM electrolyzer further tolerated dynamic operation relevant to renewable power inputs. Under alternating current densities of 0.5 and 1.0 A cm^{-2}, it showed rapid and reproducible voltage responses without discernible voltage drift during the prolonged variable-load test (Fig. 5c). It also maintained stable responses during high-frequency start-stop cycling between 1.0 and 0.1 A cm^{-2}, with each stage held for 15 min (Fig. 5d). These results indicate that the integrated interface can withstand repeated changes in gas evolution, electrolyte redistribution and interfacial stress. Product quantification validated the Faradaic nature of the electrolytic process, as the measured H_2 and O_2 production rates closely matched theoretical values, and the H_2 production rate remained essentially unchanged after 5,000 h of operation (Fig. 5e).

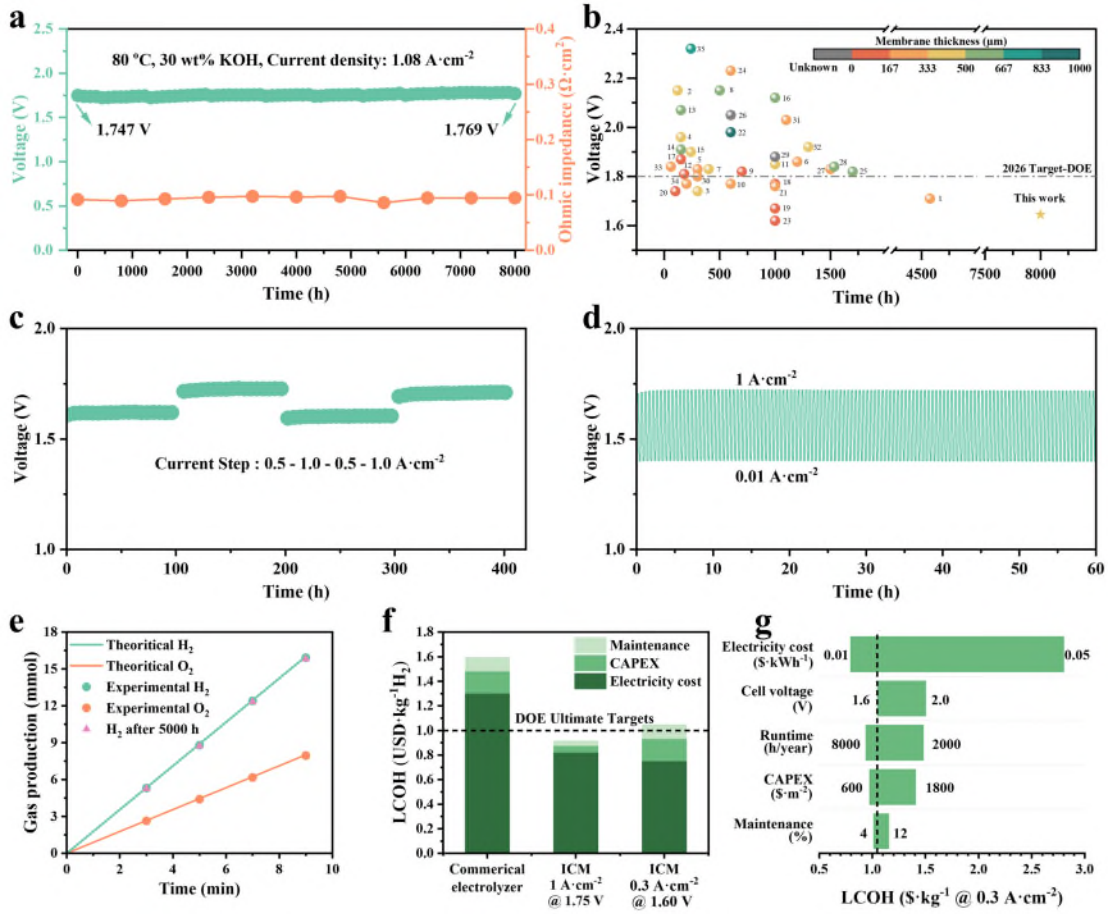


Fig. 5 Durability and economic assessment of the ICM-based electrolyzer. a, Cell voltage and ohmic resistance during long-term galvanostatic operation at a high current density of 1.08 A cm^{-2}. **b,** Comparison of membrane thickness and stability test duration with recently reported alkaline water electrolysis systems. **c,** Stability under alternating current densities of 0.5 and 1.0 A cm^{-2}, with each step maintained for 100 h. **d,** High frequency start-stop cycling between 0.1 and 1.0 A cm^{-2}, with each step maintained for 15 min. **e,** Theoretical and measured H_2 and O_2 production, including H_2 production after 5,000 h of operation. **f,** LCOH comparison between a commercial electrolyzer and the ICM-based electrolyzer operated at 1.0 A cm^{-2} at 1.75 V and 0.3 A cm^{-2} at 1.60 V. **g,** Sensitivity analysis of the LCOH of the ICM-based electrolyzer operated at 0.3 A cm^{-2}.

Finally, the levelized cost of hydrogen (LCOH) was estimated to evaluate whether the electrochemical advantages of the ICM translate into economic benefits. At an electricity price of US$0.015 kWh^{-1}, the commercial reference electrolyzer exhibited an LCOH of US$1.596 kg^{-1} H_2, whereas the ICM electrolyzer operated at 1.0 A cm^{-2} and 1.75 V reduced the LCOH to US$0.915 kg^{-1} H_2, below the DOE Hydrogen Shot target of US$1 kg^{-1} H_2 (Fig. 5f). Operation at 0.3 A cm^{-2} and 1.60 V gave a slightly

higher LCOH of US$1.046 kg^{-1} H_2, despite the lower cell voltage, because the lower hydrogen-production rate increased the capital-cost contribution per unit hydrogen. Sensitivity analysis identified electricity price as the dominant factor affecting LCOH, followed by cell voltage, annual operating time, capital cost and maintenance cost (Fig. 5g). These results show that high current density, low cell voltage and high annual utilization must be considered together to minimize hydrogen-production cost, and that the ICM provides both energy-efficiency and capital-utilization advantages for cost-effective alkaline water electrolysis.

Conclusion

In summary, we developed an integrated catalyst-membrane, denoted as ICM, for liquid alkaline water electrolysis by replacing the mechanically contacted catalyst-membrane boundary in conventional zero-gap cells with a structurally continuous interface. Coupled phase inversion of a NiAl catalyst layer and a ZrO_2-polysulfone membrane produced a monolithic asymmetric architecture that combines a porous catalytic region, finger-like ion-transport channels and a compact gas-barrier skin. This architecture preserved membrane-level ionic conductivity while improving wettability and resistance to gas penetration.

Comparison with a catalyst-laminated membrane of similar composition established interfacial continuity as the key origin of the performance improvement. By eliminating the discrete laminated boundary and associated voids, the ICM suppressed interfacial bubble retention, avoided the current-dependent increase in ohmic resistance and reduced H_2 crossover by limiting local gas enrichment at the catalyst-membrane interface. Polarization-curve deconvolution further showed that the performance gain arose mainly from reduced ohmic loss rather than enhanced intrinsic catalyst activity.

The optimized ICM electrolyzer required 1.65 V to reach 1.0 A cm^{-2} and delivered 2.05 A cm^{-2} at 1.80 V. It operated for more than 8000 h at 1.08 A cm^{-2} with a degradation rate of 1.9 μV h^{-1}, corresponding to a projected lifetime of approximately 92,000 h under the adopted degradation-rate assumption. Under the same economic framework, ICM operation reduced the calculated levelized cost of hydrogen to US$0.915 kg^{-1} H_2 at an electricity price of US$0.015 kWh^{-1}. Together, these findings establish catalyst-membrane interfacial continuity as a critical design parameter for high current density, low-cost alkaline water electrolysis, beyond the conventional focus on catalyst activity and membrane resistance alone.

Methods

Materials

Potassium hydroxide (KOH, GR, ≥85%), polyvinylpyrrolidone (PVP, average M_w 58000, K29-32), potassium sodium tartrate tetrahydrate ($C_4H_4O_6KNa·4H_2O$, AR, ≥99%), N-methylpyrrolidone (NMP, electronic grade, ≥99.9%), $Co(NO_3)_2·6H_2O$ (AR, ≥99%), $Ni(NO_3)_2·6H_2O$ (AR, ≥98%), $FeSO_4·7H_2O$ (AR, ≥99%) and urea (AR, ≥99%) were purchased from Aladdin and used as received. Ultrapure water (18.2 MΩ·cm) was produced in the laboratory. Polysulfone (PSU, P-1700NTLCD, M_w 67,000-72,000) was purchased from Syensqo SA/NV. Zirconium oxide (ZrO_2, 20 nm, 99%) were purchased from Jinan Zhiding New Materials Co., Ltd. Ni foam (0.5 mm, porosity 95%) and Ni felt (SNi025, 0.25 mm, porosity 65%) were purchased from Suzhou Sinero Technology Co., Ltd. Ni mesh (0.5 mm, 46-mesh) and RaneyNi (0.6 mm, 46-mesh Ni mesh substrate) were purchased from Suzhou Baoshilai New Materials Co., Ltd. Nickel aluminum alloy particles (Ni:Al = 1:1, D90 = 42 μm) were purchased from Zhejiang Fumei Alloy Co., Ltd. Zirfon UTP 500 was purchased from Agfa-Gevaert. Polyphenylene sulfide membrane (PPS, 0.8 mm) was purchased from Toray Industries, Inc., Japan.

Preparation of ICM

A binder solution was first prepared by dissolving 4.0 g of PSU and 0.63 g of PVP in 25.4 g of NMP under continuous stirring until complete dissolution. A predetermined amount of Ni-Al alloy powder was then added to the binder solution, and the mixture was stirred at 1,000 rpm for 30 min in a thermostatic water bath maintained at 25 °C to obtain the catalyst slurry. The coating stage was heated to 60 °C, and the doctor-blade gap was adjusted to the desired value. The catalyst slurry was subsequently cast onto a glass plate and dried to form the initial catalyst layer. A separate binder solution was prepared by dissolving 6.3 g of PSU and 1.0 g of PVP in 40 g of NMP, followed by the addition of 32 g of ZrO_2. The resulting mixture was stirred at 600 rpm for 24 h and subsequently degassed under vacuum for 10 min to obtain the membrane slurry. The coating stage was maintained at 40 °C, and the blade gap was set to 750 μm. The membrane slurry was then cast directly onto the glass plate bearing the preformed catalyst layer. After pre-evaporation for 5 min, the resulting bilayer precursor was completely immersed in deionized water for phase inversion for 24 h, with the water replaced every 8 h. Following phase inversion, the solidified membrane was removed

from the water bath and dried in an oven at 80 °C for 30 min to obtain the catalyst-coated membrane (ICM).

Peparation of ZP membrane

A binder solution was prepared by dissolving 6.3 g of PSU and 1.0 g of PVP in 40 g of NMP under continuous stirring. Subsequently, 32 g of ZrO_2 was added, and the resulting mixture was stirred at 600 rpm for 24 h, followed by vacuum degassing for 10 min to obtain a homogeneous membrane slurry. The coating stage was maintained at 40 °C, and the casting gap was set to 750 μm. The membrane slurry was then cast directly onto a clean glass plate and allowed to pre-evaporate for 5 min. The coated glass plate was completely immersed in deionized water for phase inversion for 24 h, with the water replaced every 8 h. After phase inversion, the solidified membrane was removed from the water bath and dried at 80 °C for 30 min. The resulting ZrO_2-polysulfone membrane was denoted as ZP.

Peparation of CLM

A binder solution was prepared by dissolving 4.0 g of PSU and 0.63 g of PVP in 25.4 g of NMP under continuous stirring. A predetermined amount of Ni-Al alloy powder was then added, and the mixture was stirred at 1,000 rpm for at least 30 min in a thermostatic water bath maintained at 25 °C to obtain the catalyst slurry. The coating stage was heated to 60 °C, and the casting gap was adjusted to the desired value. The catalyst slurry was subsequently cast onto a glass plate and dried to form the initial catalyst layer. After activation, the resulting catalyst film was placed in direct contact with the membrane surface. The assembled catalyst layer and membrane were sandwiched between two 0.1 mm PTFE release films to prevent adhesion to the platens and then transferred to a flat-plate hot press. Hot pressing was conducted at 120 °C and 5 MPa for 5 min. After removal of the PTFE films, the catalyst-laminated membrane (CLM) was obtained.

Peparation of CoNiFe@NF

Nickel foam was cut into pieces measuring 2.4 cm × 2.4 cm. Before use, the nickel foam was immersed in 1 M HCl for 15 min to remove the surface oxide layer and attached impurities. It was then sequentially ultrasonicated in deionized water and ethanol for 15 min each, followed by drying in a vacuum oven at 50 °C. $Co(NO_3)_2 \cdot 6H_2O$ (700 mg), $Ni(NO_3)_2 \cdot 6H_2O$ (500 mg), $FeSO_4 \cdot 7H_2O$ (111.2 mg) and urea (900 mg) were dissolved in 70 ml of ethanol under vigorous stirring to obtain a homogeneous precursor suspension. The precursor suspension was transferred into a Teflon-lined stainless-steel

autoclave, and the pretreated nickel foam was completely immersed in the solution. The autoclave was sealed and heated at 120 °C for 6 h. After naturally cooling to room temperature, the resulting electrode was thoroughly washed with deionized water and ethanol and dried at room temperature. The obtained electrode was denoted as CoNiFe@NF.

Characterizations

The surface and cross-sectional morphologies of the samples were characterized using a Quattro S scanning electron microscope (SEM, Thermo Fisher Scientific, USA). To further investigate the phase composition and microstructure of the catalyst particles, an electron-transparent lamella was prepared from the ICM by focused ion beam milling (FIB, Crossbeam 540, Carl Zeiss Microscopy GmbH, Germany) and subsequently examined by transmission electron microscopy (TEM, Tecnai G2 F20 S-TWIN, FEI Company, USA). Elemental distributions were analyzed by energy-dispersive X-ray spectroscopy (EDS) using an X-MaxN 80T detector (Oxford Instruments NanoAnalysis, UK). X-ray photoelectron spectroscopy (XPS) measurements were performed using a K-Alpha spectrometer equipped with a monochromatic Al Kα X-ray source (Thermo Fisher Scientific, USA). X-ray diffraction (XRD) patterns were recorded using a D8 ADVANCE diffractometer (Bruker, Germany) with Co Kα radiation over a 2θ range of 10-90° at a scan rate of 5° min^{-1} at room temperature. Fourier transform infrared (FTIR) spectroscopy was performed using a Spectrum instrument (PerkinElmer Inc., USA). Water contact angles were measured using an OCA 25 optical contact-angle and drop-shape analysis system (DataPhysics Instruments GmbH, Germany). Bubble adhesion forces were measured in water using a DCAT 25 dynamic contact-angle analyzer and force tensiometer (DataPhysics Instruments GmbH, Germany). Bubble-point pressure (BPP) and pore-size distribution was measured using a pore-size analyzer (BSD-PB).

Water uptake was determined gravimetrically. The samples were dried to a constant mass and weighed to obtain the dry mass, m_{dry}. They were then immersed in deionized water for 30 min, removed, gently blotted to remove excess surface water and immediately weighed to obtain the wet mass, m_{wet}. The water-uptake ratio was calculated as:

$$Water\ uptake = \frac{m_{wet} - m_{dry}}{m_{dry}} \times 100\% \quad (1)$$

The through-plane area-specific resistance of the membrane samples was measured in an H-type cell filled with 30 wt% KOH using an electrochemical workstation (EnergyLab XM, Solartron Analytical, UK). Electrochemical impedance spectra were collected over a frequency range of 50 kHz to 0.5 Hz at 25 °C. The membrane area-specific resistance was obtained by subtracting the resistance of the empty cell (R_1) from that measured with the sample installed (R_2). The effective through-plane ionic conductivity was calculated as:

$$\sigma = \frac{L}{A \times (R_2 - R_1)} \tag{2}$$

where L is the sample thickness, and A is the effective area of the membrane exposed to the electrolyte.

Electrochemical characterization

The hydrogen evolution reaction (HER) and oxygen evolution reaction (OER) activities were evaluated in 1 M KOH at 25 °C using a CHI760D electrochemical workstation. Measurements were conducted in a conventional three-electrode configuration, with the as-prepared electrode (1 cm × 1 cm) as the working electrode, a Ni sheet for HER or a Pt sheet for OER as the counter electrode, and a Hg/HgO electrode as the reference electrode. Before each measurement, the electrolyte was purged with high purity H_2 for HER or O_2 for OER for 15 min to remove residual air and establish the corresponding gas-saturated conditions. Linear sweep voltammetry was performed at a scan rate of 10 mV s^{-1} with 85% iR compensation. All measured potentials were converted to the reversible hydrogen electrode (RHE) scale according to:

$$E_{\mathrm{RHE}} = E_{\mathrm{Hg/HgO}} + E^0_{\mathrm{Hg/HgO}} + 0.0591\,\mathrm{pH} \tag{3}$$

where $E^0_{\mathrm{Hg/HgO}}$ is the potential of the Hg/HgO reference electrode relative to the standard hydrogen electrode. For a Hg/HgO reference electrode containing 1 M KOH, $E^0_{\mathrm{Hg/HgO}}$ was taken as 0.098 V at 25 °C.

For alkaline water electrolysis measurements, the membrane was first immersed in KOH solution for 24 h. Subsequently, the membrane was sandwiched between the cathode (PTL) and anode, which were positioned between two 316 L stainless steel bipolar plates. PTFE gaskets were used to prevent electrolyte and gas leakage and to electrically isolate the two bipolar plates, thereby avoiding short-circuiting. Finally, all components were securely fastened together using bolts and nuts. The electrolysis

performance was evaluated using a custom-designed electrolyzer system comprising dual gas-liquid separation tanks for anode and cathode compartments, peristaltic pumps, an electrolyte heating unit, temperature control system, and power supply unit. The active electrode area was 2.4 cm × 2.4 cm. Current-voltage characteristics were measured using a LANHE D340A power supply, while electrochemical impedance spectra (EIS) was collected using a Solartron ENERGYLAB XM. EIS measurements were carried out with an AC perturbation current of 15% of the DC current at frequencies ranging from 50 kHz to 0.5 Hz. All alkaline water electrolysis tests were conducted at 80 ^{o}C in 30 wt% KOH solution, with two peristaltic pumps delivering electrolyte to the anode and cathode at 45 mL min^{-1} each.

Hydrogen crossover measurement

The hydrogen concentration in the oxygen product gas (H_2-in-O_2, HTO) was monitored online using an A91 Plus gas chromatograph (Pannatek Instruments, China). The O_2 leaving the anodic gas-liquid membrane was passed sequentially through a gas-washing bottle and a drying tube to remove entrained electrolyte and moisture before being continuously introduced into the gas chromatograph. The H_2 concentration was determined from the calibrated chromatographic response and reported as the volume percentage of H_2 in the oxygen product gas.

Deconvolution of the polarization curves

The cell voltage was deconvoluted into thermodynamic, kinetic, ohmic and mass-transport-related contributions. The total overpotential at a given current density was calculated as:

$$\eta_{\text{total}} = V_{\text{cell}} - E_{\text{rev}} \tag{4}$$

where V_{cell} is the measured cell voltage and E_{rev} is the reversible voltage for water electrolysis.

The kinetic overpotential was obtained by fitting the low-current-density region of the polarization curve, where ohmic and mass transport losses were assumed to be negligible, using the Tafel relationship:

$$\eta_{\text{kin}} = a + b\log_{10} j \tag{5}$$

where a is the intercept, b is the Tafel slope and j is the current density in A cm^{-2}. The fitting was performed in the current-density region below 50 mA cm^{-2}.

The ohmic overpotential was calculated from the high-frequency resistance obtained from the corresponding EIS spectrum:

$$\eta_{\text{ohm}} = jR_{\text{HFR}} \tag{6}$$

where RHFRis the area-specific high-frequency resistance in Ω cm^2. The residual contribution was assigned to mass transport losses:

$$\eta_{\text{mass}} = \eta_{\text{total}} - \eta_{\text{kin}} - \eta_{\text{ohm}} \tag{7}$$

Theoretical hydrogen production and Faradaic efficiency

The theoretical amount of hydrogen generated was calculated according to Faraday's law:

$$n_{\text{H}_2,\text{theo}} = \frac{It}{2F} \tag{8}$$

where $n_{\text{H}_2,\text{theo}}$ is the theoretical amount of H_2 in mol, I is the operating current in A, t is the electrolysis time in s and F is the Faraday constant (96,485.3 C mol^{-1}).

The theoretical hydrogen volume under standard conditions was calculated as:

$$V_{\text{H}_2,\text{theo}} = n_{\text{H}_2,\text{theo}} V_{\text{m}} \tag{9}$$

where $V_{\text{m}} = 22.43 \times 10^{-3}$ Nm^3 mol^{-1} is the molar volume of an ideal gas under standard conditions.

The Faradaic efficiency was calculated as:

$$\text{FE}_{\text{H}_2} = \frac{V_{\text{H}_2,\text{meas}}}{V_{\text{H}_2,\text{theo}}} \times 100\% \tag{10}$$

Similarly, the oxygen Faradaic efficiency was calculated as:

$$\text{FE}_{\text{O}_2} = \frac{V_{\text{O}_2,\text{meas}}}{V_{\text{O}_2,\text{theo}}} \times 100\% \tag{11}$$

Specific electricity consumption for hydrogen production

The specific electricity consumption for hydrogen production was calculated from the cell voltage and the theoretical electric charge required to generate 1 Nm^3 of H_2. Taking the standard molar gas volume as 22.43 L mol^{-1}, the unit electric charge was calculated to be 2,390 Ah $Nm^{-3}H_2$. Accordingly, the specific electricity consumption was calculated as $W = 2.39\ V_{\text{cell}}$, where W is expressed in kWh $Nm^{-3}H_2$.

Lattice Boltzmann simulation

The hydrogen crossover behaviour was simulated using an in-house C++ code developed in Visual Studio based on the D2Q9 lattice Boltzmann method and a pseudopotential multiphase model. A prescribed inlet velocity was applied, with a constant-pressure boundary at the top and periodic boundaries on the left and right sides. Two interfacial configurations were considered: Case A (ICM), in which the catalyst

layer was in direct contact with the membrane, and Case B (CLM), in which a 10 μm gap was introduced between the catalyst layer and membrane. The simulations were used to compare hydrogen accumulation and transport in the integrated and gapped interfaces.

Techno-economic analysis

A steady-state techno-economic model was used to estimate the levelized cost of hydrogen (LCOH) for a commercial alkaline electrolyzer and two integrated catalyst–membrane (ICM) operating cases. All scenarios assumed a system lifetime of 20 years, an annual operating time of 5,000 h and a nominal hydrogen production capacity of 1,000 Nm^3H_2 h^{-1}. The commercial electrolyzer was operated at 2.00 V and 0.3 A cm^{-2}, whereas the ICM electrolyzer was evaluated at 1.75 V and 1.0 A cm^{-2} and at 1.60 V and 0.3 A cm^{-2}. A Faradaic efficiency of 95% was used for all cases. The overall energy-efficiency factors were set to 65% for the commercial electrolyzer and 90% for the ICM cases.

The total operating current required to achieve the specified hydrogen production rate was calculated from Faraday's law:

$$I = \frac{2FV_{\mathrm{H_2}}}{3600V_{\mathrm{m}}\eta_{\mathrm{F}}} \tag{12}$$

where I is the total operating current, F is the Faraday constant (96,485.3 C mol^{-1}), V_{H_2} is the hydrogen production rate in Nm^3 h^{-1}, V_m is the standard molar gas volume (0.0224 Nm^3 mol^{-1}) and is the Faradaic efficiency.

The theoretical water-consumption rate was determined from the stoichiometry of water electrolysis:

$$V_{\mathrm{H_2O}} = \frac{V_{\mathrm{H_2}} M_{\mathrm{H_2O}}}{V_{\mathrm{m,k}} \rho_{\mathrm{H_2O}}} \tag{13}$$

where, $M_{H_2O} = 18\ \mathrm{kg\ kmol^{-1}}$, $V_{\mathrm{m,k}} = 22.4\ \mathrm{Nm^3\ kmol^{-1}}$, and $\rho_{H_2O} = 1{,}000\ \mathrm{kg\ m^{-3}}$. At a hydrogen production rate of 1,000 Nm^3 h^{-1}, the theoretical water-consumption rate was 0.804 m^3 h^{-1}.

Capital expenditure was estimated from the total active area. The area-specific stack cost was set to US$800 m^{-2}, and the installation factor was set to 1.2:

$$C_{\mathrm{installed}} = f_{\mathrm{inst}} C_{\mathrm{stack}} = f_{\mathrm{inst}} c_{\mathrm{stack,A}} A \tag{14}$$

where, C_{stack} is the total stack cost, f_{inst} the installation factor, set to 1.2, $c_{\mathrm{stack,A}}$ is the

area-specific stack cost, set to US\$800 m^{-2}, and A is the total active electrolyzer area.

The land and balance-of-plant cost and hydrogen-purification equipment cost were each assumed to be 15% of the installed electrolyzer cost. The total capital expenditure was therefore calculated as:

$$C_{\mathrm{CAPEX}} = C_{\mathrm{installed}} + C_{\mathrm{BOP}} + C_{\mathrm{pur}} \tag{15}$$

Annual operating expenditure included electricity, maintenance and water costs. An industrial electricity price of US\$0.015 kWh^{-1} and a water price of US\$0.70 m^{-3} were assumed. The annual electricity cost was calculated as:

$$C_{\mathrm{electricity}} = \frac{P t_{\mathrm{op}} p_{\mathrm{e}}}{\eta_{\mathrm{E}}} \tag{16}$$

where t_{op} is the annual operating time, p_{e} is the electricity price and η_{E} is the overall energy-efficiency factor. Annual maintenance expenditure was assumed to be 6% of the installed electrolyzer cost:

$$C_{\mathrm{maintenance}} = f_{\mathrm{m}} C_{\mathrm{installed}} \tag{17}$$

The annual water cost was calculated as:

$$C_{\mathrm{water}} = V_{\mathrm{H_2O}} t_{\mathrm{op}} p_{\mathrm{w}} \tag{18}$$

The total annual operating expenditure was:

$$C_{\mathrm{OPEX}} = C_{\mathrm{electricity}} + C_{\mathrm{maintenance}} + C_{\mathrm{water}} \tag{19}$$

The initial capital investment was annualized using a capital recovery factor:

$$\mathrm{CRF} = \frac{r(1+r)^n}{(1+r)^n - 1} \tag{20}$$

where r is the annual discount rate, set to 4.5%, and n is the system lifetime. The corresponding CRF was 0.0769 yr^{-1}. The total annualized cost was calculated as:

$$C_{\mathrm{annual}} = C_{\mathrm{CAPEX}} \mathrm{CRF} + C_{\mathrm{OPEX}} \tag{21}$$

Annual hydrogen production on mass bases was calculated as:

$$m_{\mathrm{H_2,annual}} = V_{\mathrm{H_2,annual}} \frac{M_{\mathrm{H_2}}}{V_{\mathrm{m,k}}} = V_{\mathrm{H_2}} t_{\mathrm{op}} \frac{M_{\mathrm{H_2}}}{V_{\mathrm{m,k}}} \tag{22}$$

where $M_{\mathrm{H_2}} = 2\ \mathrm{kg\ kmol^{-1}}$.

The mass-based LCOH values were then obtained from:

$$\mathrm{LCOH} = \frac{C_{\mathrm{annual}}}{m_{\mathrm{H_2,annual}}} \tag{23}$$

For sensitivity analysis, individual operating or economic parameters were varied

while all other baseline assumptions were held constant, and the LCOH was recalculated using the same model.

Data availability

The data that support the findings of this study are available within the article and its Supplementary Information. Source data are provided with this paper.

Reference

1 Rocha, F. *et al.* Proton exchange membrane-like alkaline water electrolysis using flow-engineered three-dimensional electrodes. *Nature Communications* **15** (2024).

2 Liu, Y. *et al.* Janus electronic state of supported iridium nanoclusters for sustainable alkaline water electrolysis. *Nature Communications* **15** (2024).

3 Li, W. *et al.* Zwitterion-Modified NiFe OER Catalyst Achieving Ultrastable Anion Exchange Membrane Water Electrolysis via Dynamic Alkaline Microenvironment Engineering. *Angewandte Chemie-International Edition* **64** (2025).

4 Wan, L. *et al.* Key components and design strategy of the membrane electrode assembly for alkaline water electrolysis. *Energy & Environmental Science* **16**, 1384-1430 (2023).

5 Wu, Y., Xu, G., Zhou, J. & Cao, D. Research progress of the porous membranes in alkaline water electrolysis for green hydrogen production. *Chemical Engineering Journal* **505** (2025).

6 Han, S. *et al.* Dynamic polarization control of Ni electrodes for sustainable and scalable water electrolysis under alkaline conditions. *Nature Communications* **16** (2025).

7 Chen, X. *et al.* Ce Single Atom-Engineered Amorphous/Crystalline Nanosheets for Enhanced Alkaline Water Electrolysis. *Advanced Materials* **37** (2025).

8 You, J. *et al.* A rationally thin composite membrane with differentiated pore structure for industrial-scale alkaline water electrolysis. *Nature Communications* **16** (2025).

9 Xu, Z. *et al.* Uniform nanoporous zirconia composite membrane enabling high-performance alkaline water electrolysis. *Nature Communications* (2026).

10 Gao, Z. *et al.* Sulfonated-PPS/LDH Composite Membrane With Hydrogen Bond Network for High-Performance Alkaline Water Electrolysis. *Small* **22** (2026).

11 Liao, Y., Deng, G., Ding, L. & Wang, H. A thin and flexible composite membrane with low area resistance and high bubble point pressure for advanced alkaline water electrolysis. *Journal of Membrane Science* **689** (2024).

12 Henkensmeier, D. *et al.* Separators and Membranes for Advanced Alkaline Water Electrolysis. *Chemical Reviews* **124**, 6393–6443 (2024).

13 Li, X. *et al.* Lewis Acid-Base Molecular Anchoring Through Oxygen Vacancies Enables Ultrastable and High-Conductivity Membranes for Alkaline Water Electrolysis. *Advanced Energy Materials* **16** (2026).

14 Liao, Y., Deng, G., Wu, H., Ding, L. & Wang, H. A Porous Skeleton-Supported Organic/Inorganic Composite Membrane for High-Efficiency Alkaline Water Electrolysis. *Advanced Functional Materials* **34** (2024).

15 Song, W. *et al.* Multilayer-structure reinforced composite membrane coupled with etched ZrO_2 nanoparticles for enhanced efficiency in alkaline water electrolysis. *Journal of Membrane Science* **727** (2025).

16 Song, W. *et al.* ZrO_2 nanofibers/sulfonated polysulfone-polysulfone composite membrane: Achieving efficient alkaline water electrolysis through multivariable

synergistic regulation. *Journal of Membrane Science* **735** (2025).
17 Ikhsan, M. M. *et al.* Sulfonated polybenzimidazole for low-alkalinity ion solvating membrane water electrolysis. *Nature Energy* **10**, 1347–1359 (2025).
18 Wang, G. *et al.* Probing Electrode Transformation under Dynamic Operation for Alkaline Water Electrolysis. *Advanced Energy Materials* **15** (2025).
19 Wan, L. *et al.* Oriented intergrowth of the catalyst layer in membrane electrode assembly for alkaline water electrolysis. *Nature Communications* **13** (2022).
20 Song, W. *et al.* Novel high-safety composite separator: Achieving efficient alkaline water electrolysis by compositing microporous polysulfone membrane on one side of complete structure polyphenylene sulfide fabric. *Chemical Engineering Journal* **503** (2025).
21 Zhou, C. *et al.* Synergistic membrane-electrode engineering for high-performance alkaline water electrolysis. *Chemical Engineering Science* **316** (2025).
22 Liu, Y. *et al.* A rolling strategy for layered double hydroxide membrane to boost alkaline water electrolysis. *Journal of Membrane Science* **720** (2025).
23 Zhang, Q. *et al.* Toward Energy-Efficient Alkaline Water Electrolysis: Advances in Mass Transport Optimization and Electrolyzer Design. *Advanced Energy Materials* **16** (2026).
24 Song, W. *et al.* Synergistic Engineering of Ethyl Cellulose and Etched ZrO_2 Nanoparticles for Tailored Microporous Composite Membranes Toward Efficient Alkaline Water Electrolysis. *Advanced Functional Materials* **36** (2026).
25 Wu, L. *et al.* Bubble dynamics matters at high-rate water electrolysis. *Nature Communications* **17** (2026).
26 Li, L. *et al.* High-Rate Alkaline Water Electrolysis at Industrially Relevant Conditions Enabled by Superaerophobic Electrode Assembly. *Advanced Science* **10** (2023).
27 Kuang, W. *et al.* Self-Supported Ni/$Ni(OH)_2$ Electrodes for High-Performance Alkaline and AEM Water Electrolysis. *Advanced Energy Materials* **15** (2025).
28 Diao, S. *et al.* Highly durable porous NiO-derived electrodes with superior bifunctional activity for scalable alkaline water electrolysis. *Chemical Engineering Journal* **504** (2025).
29 Zhang, R. *et al.* Pt modified Ni-PES membrane for simultaneous hydrogen production and separation via alkaline water electrolysis. *Journal of Membrane Science* **742** (2026).
30 Wan, L., Xu, Z., Xu, Q., Wang, P. & Wang, B. Overall design of novel 3D-ordered MEA with drastically enhanced mass transport for alkaline electrolyzers. *Energy & Environmental Science* **15**, 1882-1892 (2022).

Acknowledgements

This work was supported by the Beijing Natural Science Foundation-Chaoyang Joint Fund (Grant No. L2609045), the National Natural Science Foundation of China (Grant No. 52202234), and the Young Elite Scientists Sponsorship Program by BAST (Grant No. BYESS2023073) received by T.Y.

CRediT authorship contribution statement

SK.D and SL.L contributed equally to this work. SK.D and SL.L conceived and designed the research. SL.L and ZH.L performed fabrication and characterization.

SK.D performed cell testing, analyzed data and wrote the manuscript. Y.L assisted in the characterization and analyzed data. TR.Y. conceived the study, curated the data, developed the methodology, acquired funding, supervised the work, and reviewed and edited the manuscript. JG.L. provided resources, supervised the work, and reviewed and edited the manuscript. All authors discussed the results and reviewed the manuscript.

Declaration of competing interest

The authors declare that they have no known competing financial interests or personal relationships that could have appeared to influence the work reported in this paper.

Supplementary Files

This is a list of supplementary files associated with this preprint. Click to download.

- SI.docx